Laboratory and theoretical modeling of air-sea momentum transfer under severe wind conditions

Y. I. Troitskaya,[1,2] D. A. Sergeev,[1,2] A. A. Kandaurov,[1,2] G. A. Baidakov,[1,2] M. A. Vdovin,[1,2] and V. I. Kazakov[1,2]

Received 26 November 2011; revised 31 March 2012; accepted 8 May 2012; published 27 June 2012.

[1] The laboratory experiments on investigation of aerodynamic resistance of the waved water surface under severe wind conditions (up to $U_{10} \approx 40$ m s^{-1}) were carried out, complemented by measurements of the wind-wave spectra. The tendency to saturation of the surface drag was observed for wind speeds exceeding 25 m s^{-1}, accompanied by the saturation of wind-wave slopes. The effect of surface drag saturation can be explained quantitatively within the quasi-linear model of the air boundary layer above the waved water surface, when the contribution of the short-wave part of the wind-wave spectrum to aerodynamic resistance of the water surface is taken into account.

Citation: Troitskaya, Y. I., D. A. Sergeev, A. A. Kandaurov, G. A. Baidakov, M. A. Vdovin, and V. I. Kazakov (2012), Laboratory and theoretical modeling of air-sea momentum transfer under severe wind conditions, *J. Geophys. Res.*, *117*, C00J21, doi:10.1029/2011JC007778.

1. Introduction

[2] One of the main characteristics appearing in the models of forecasting wind over the sea is air-sea momentum transfer determined by the parameters of the wind waves and quantitatively parameterized by the sea surface drag coefficient C_D. For definition C_D, we introduce the turbulent shear stress or turbulent momentum flux beyond the wave boundary layer

$$\tau_{turb}(z) = \rho_a u_*^2, \tag{1}$$

where ρ_a is the air density, u_* is the wind friction velocity. At the distance from the water surface much less compared to the Monin-Obukhov length determined by density stratification of atmospheric boundary layer, the wind is the turbulent boundary layer with the logarithmic mean velocity profile

$$U(z) = \frac{u_*}{\kappa} \ln \frac{z}{z_0}. \tag{2}$$

[3] Similar to the resistance law of the wall turbulent flow the sea surface drag coefficient is introduced as follows:

$$C_D = \frac{\tau_{turb}}{\rho_a U_{10}^2} = \frac{u_*^2}{U_{10}^2}, \tag{3}$$

where U_{10} is the wind velocity at a standard meteorological height $H_{10} = 10$ m. Bulk formulas, which relate C_D to U_{10} are obtained either by compilation of empirical data [*Large and Pond*, 1981; *Taylor and Yelland*, 2001; *Fairall et al.*, 2003] or by numerical modeling [see, e.g., *Janssen*, 1989, 1991; *Makin et al.*, 1995; *Hara and Belcher*, 2004]. Numerous field measurements give increasing dependencies of C_D on the wind speed, which is associated with the increase of wave heights with the wind.

[4] The aerodynamic drag coefficient of the sea surface is a critical parameter in the theory of tropical hurricanes: it is of special interest now in connection with the problem of explanation of the sea surface drag saturation at the wind speed exceeding 30 m s^{-1}. The idea of saturation (and even reduction) of the coefficient of aerodynamic resistance of the sea surface at hurricane wind speed was first suggested by *Emanuel* [1995] on the basis of theoretical analysis of sensitivity of maximum wind speed in a hurricane to the ratio of the enthalpy and momentum exchange coefficients. Both field [*Powell et al.*, 2003; *Jarosz et al.*, 2007] and laboratory [*Donelan et al.*, 2004] experiments confirmed that despite the increase in surface wave heights at hurricane wind speed the sea surface drag coefficient is significantly reduced as compared with the parameterization obtained at moderate to strong wind conditions [*Taylor and Yelland*, 2001; *Fairall et al.*, 2003].

[5] Two groups of theoretical models were suggested to explain the effect of the sea surface drag reduction during hurricane winds. The first group of models [*Kudryavtsev and Makin*, 2007; *Kukulka et al.*, 2007] explains the sea surface drag reduction by the peculiarities of the airflow over breaking waves, which determine the form drag of the sea surface. Similarly, in *Donelan et al.* [2004] the stabilization of the drag coefficient is qualitatively explained by a change in the shape of the surface elevation in dominant waves at

[1]Institute of Applied Physics, Russian Academy of Sciences, Nizhni Novgorod, Russia.
[2]Radiophysics Department, Lobachevsky State University of Nizhni Novgorod, Nizhni Novgorod, Russia.

Corresponding author: Y. I. Troitskaya, Institute of Applied Physics, Russian Academy of Sciences, Ulyanova Str. 46, 603950 Nizhni Novgorod, Russia. (yuliya@hydro.appl.sci-nnov.ru)

0148-0227/12/2011JC007778

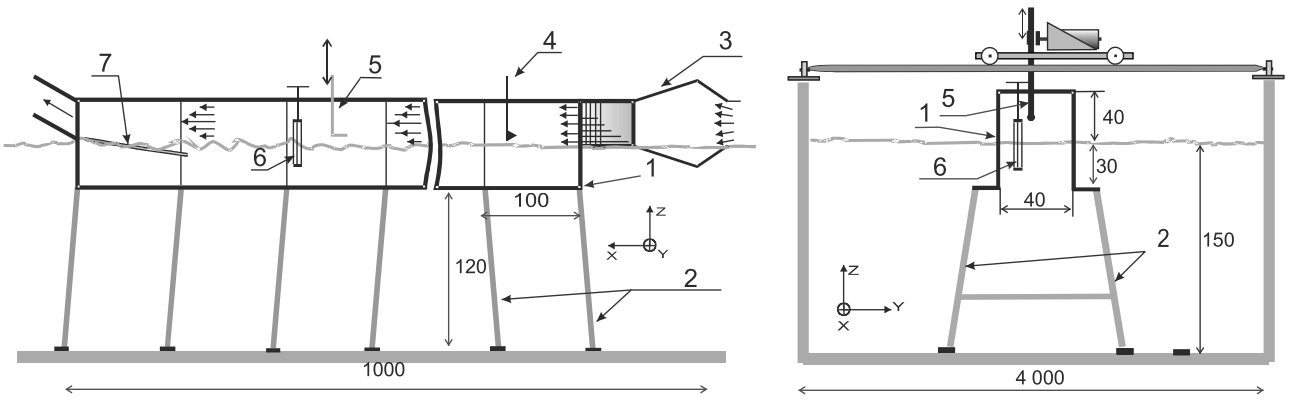

Figure 1. Sketch of experimental setup (1) straight part of flume, (2) vertical bearings, (3) expanding-narrowing section, (4) hot wire gauge, (5) Pitot tube on the scanning system, (6) three-channel string wave gauge, and (7) damping beach. All dimensions in cm.

wind velocities above 35 m s^{-1}, which is accompanied by the occurrence of a steep leading front. In this case the occurrence of flow separation from the crests of the waves is assumed. This assumption is based on the laboratory experiments by *Reul et al.* [1999, 2008], where airflow separation at the crests of breaking waves was observed in the instant velocity patterns by the Particle Image Velocimetry (PIV) method. A close mechanism was suggested in the paper by *Troitskaya and Rybushkina* [2008], where the sea surface drag reduction at hurricane wind speed is explained by the reduction of efficiency of wind-wave momentum exchange at hurricane conditions due to sheltering without separation.

[6] Another approach, more appropriate for the conditions of developed sea, exploits the effect of sea drops and sprays on the wind-wave momentum exchange [*Andreas and Emanuel*, 2001; *Andreas*, 2004; *Makin*, 2005; *Kudryavtsev*, 2006; *Kudryavtsev and Makin*, 2011]. *Andreas and Emanuel* [2001], *Andreas* [2004], and *Kudryavtsev and Makin* [2011] estimated the momentum exchange of sea drops and airflow, while *Makin* [2005] and *Kudryavtsev* [2006] focused on the effect of the sea drops on the stratification of the air-sea boundary layer similar to the model of turbulent boundary layer with the suspended particles by *Barenblatt and Golitsyn* [1974].

[7] In spite of the number of theoretical hypotheses, the problem of explanation of the effect of surface drag reduction at hurricane winds is not ultimately solved mostly due to the lack of experimental data. The main aim of the present work is a comprehensive study of the wind-wave interaction for the hurricane wind conditions within the laboratory experiments and theoretical modeling. The description of the experimental setup for simultaneous measurements of airflow and surface waves, peculiarities of data processing and experimental data are presented in section 2 of the present work. In section 3 the theoretical model used in this paper is described. In section 4 theoretical calculations of the surface drag coefficient are compared with the experimental data described in section 2.

2. Laboratory Modeling of the Air-Sea Interaction Under Hurricane Wind

[8] In this section we describe experimental setup, data processing and the results of new laboratory experiments devoted to the modeling of air-sea interaction at extremely strong winds.

2.1. Experimental Setup and Instruments

[9] The experiments were performed in the wind-wave flume located on top of the Large Thermostratified Tank of the Institute of Applied Physics. The principal scheme of the experimental setup is shown in Figure 1. The centrifugal fan equipped with an electronic frequency converter to control the discharge rate of the airflow produces the airflow in the flume with the straight working part of 10 m. The operating cross section of the airflow is 0.40 × 0.40 m^2, whereas the sidewalls are submerged at a depth of 0.30 m. During the experiments axis velocity in the flume varied from 5 to 25 m s^{-1} (corresponds to U_{10} from 7 m s^{-1} to 40 m s^{-1}). The wave damping beach is placed at the airflow outlet at the end of the flume.

[10] The aerodynamic resistance of the water surface was measured by the profile method at a distance of 7 m from the inlet. Wind velocity profiles were measured by the L-shaped Pitot tube with the differential pressure transducer Baratron MKS 226 A with the accuracy of 0.5% of full scale range, i.e., 3 cm s^{-1}. The lower level of scanning located at a distance of 0.5 to 1 cm from the crests of the waves and depended on the wind speed, while the upper layer was 38 cm (in 2 cm below the upper lid of the channel). The scanning method with the consecutive height increment of 3–5 mm and accruing time of 2 min at each point was used. For each fixed wind parameters, five profiles were measured for subsequent averaging.

[11] Simultaneously with the airflow velocity measurements, the wind-wave field parameters in the flume were investigated by three wire gauges positioned in the corners of an equal side triangle with 2.5 cm side, the data sampling rate was 100 Hz (see Figure 1). Three dimensional frequency-wave number spectra were retrieved from these data by the algorithm similar to *Donelan et al.* [1996] based on the window fast Fourier processing (see details below in 2.3). The experiment was accompanied by video filming of the side view of the water surface.

2.2. Peculiarities of the Profile Method for Measuring the Surface Drag Coefficient in Aerodynamic Tunnels

[12] The classical profiling method of measuring the surface drag coefficient is based on the property of the steady wall turbulent boundary layer to conserve tangential turbulent

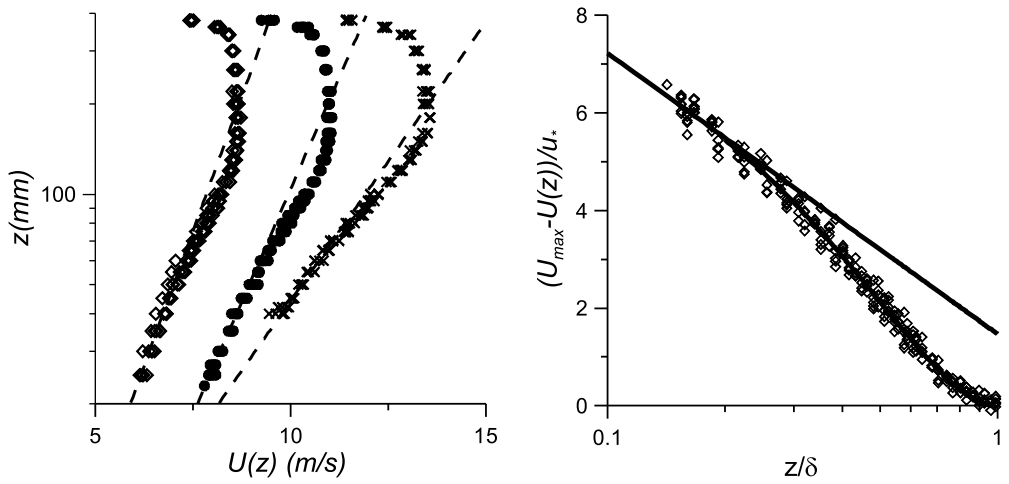

Figure 2. (left) Three examples of profiles in the aerodynamic flume over the waves for different inlet wind; dashed curves are logarithmic approximations in the layer of constant fluxes. (right) Airflow velocity profiles measured at different wind speeds over the waves in self-similar variables. The solid line is logarithmic approximation.

stress u_*^2, then the average flow velocity is logarithmic and the wind friction velocity u_* can be easily determined from (2), if the velocity profile is measured. However, developing turbulent boundary layers are typical for the aerodynamic tubes and wind flumes, then three sublayers at different distances from the water can be specified: the viscous sublayer, the layer of constant fluxes and the "wake" part (see Figure 2, left).

[13] The viscous sublayer, where viscous effects are essential, exists over the hydrodynamically smooth surfaces at the distances less than $20 \div 30\ \nu/u_*$ (ν is the kinematic viscosity), for moderate winds it is about 1 mm. The "wake" part is the outer layer of the turbulent boundary layer, where the boundary layer flow transits to the outer flow in the tube. Its thickness δ increases linearly from the inlet of the flume. The layer of constant fluxes is extended from the upper boundary of the viscous sublayer to approximately 0.15δ.

[14] Only in the layer of constant fluxes the flow velocity profile is logarithmic and can be extrapolated to the standard meteorological height H_{10}. Typically in aerodynamic tubes and wind flumes the constant layer thickness is less than 0.10 m. Measuring wind velocity profiles at the distance less than 10 cm from the wavy water surface at strong winds is a difficult problem mainly due to the effect of sprays blown from the wave crests. Fortunately, the parameters of the layer of the constant fluxes can be retrieved from the measurements in the "wake" part of the turbulent boundary layer, because the velocity profile in the developing turbulent boundary layer is described by the self-similar "law of wake" [see *Hinze*, 1959]. The self-similar variables for the velocity profile and vertical coordinates are z/δ and $(U_{\max} - U(z))/u_*$., where $U_{\max}$ is the maximum velocity in the turbulent boundary layer. The self-similar velocity profile can be approximated by the following simple equations [see *Hinze*, 1959]:

In the layer of constant fluxes

$$U_{\max} - U(z) = u_*(-2.5\ln(z/\delta) + \gamma) \tag{4}$$

In the "wake" part

$$U_{\max} - U(z) = bu_*(1 - z/d)^2. \tag{5}$$

[15] Collapse of all the experimental points in one curve in self-similar variables occurred in our experiments (see Figure 2, right). The parameters in equations (4) and (5) were obtained by the best fitting of the experimental data: $\gamma = 1.5$, $\beta = 8.5$.

[16] The parameters of the logarithmic boundary layer can be obtained from the measurements in the wake part of the turbulent boundary layer, first, retrieving the parameters of turbulent boundary layer ($U_{\max}$ and δ) from best fit of the experimental data by equation (5) and then calculating the parameters of the logarithmic boundary layer by the following expressions:

$$U(z) = 2.5u_* \ln(z/z_0), \tag{6}$$

where

$$z_0 = \delta \exp(-\kappa U_{\max}/u_* + \gamma\kappa). \tag{7}$$

Expression for C_D via measured parameters u_*, $U_{\max}$ and δ follows from equations (6) and (7):

$$C_D = \frac{\kappa^2}{(\kappa U_{\max}/u_* - \gamma\kappa + \ln(H_{10}/\delta))}. \tag{8}$$

[17] Wind velocity profiles were measured for 12 values of the axis velocity from 6 m s^{-1} to 24 m s^{-1}. C_D and U_{10} were calculated by equations (8) and (4) respectively. The obtained dependency of the surface drag coefficient on 10 m wind speed is presented in Figure 3a together with the data taken from the paper by *Donelan et al.* [2004]. The data obtained at two different facilities are rather close to each other both at the low and high wind speeds; the difference in C_D is less than 10%. The change in dependency of C_D on U_{10} is seen in both data sets at high winds, some differences,

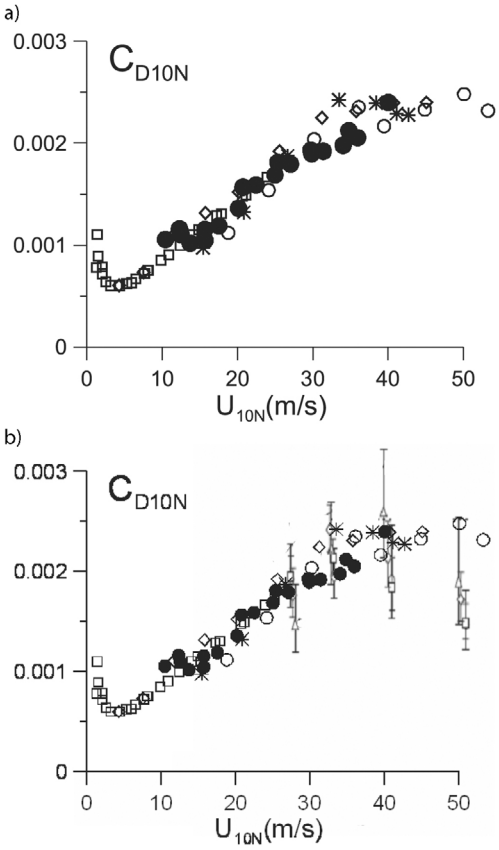

Figure 3. Surface drag coefficient. (a) Laboratory data: open symbols (squares, circles, diamonds, and asterisks) are taken from *Donelan et al.* [2004] and closed circles are measurements of the present work. (b) Compilation of the field measurements symbols with bars [*Powell et al.*, 2003] and laboratory data from Figure 3a. Figure 3a adapted from *Powell et al.* [2003] with permission from Macmillan Publishers Ltd.

apparently due to differences in the details of data processing. In *Donelan et al.* [2004] the leveling of C_D was observed for U_{10} exceeding 33 m/s. In these data a change in the angle of dependency of C_D on U_{10} occurs for U_{10} of about 25 m/s.

[18] In Figure 3b the laboratory data [*Donelan et al.*, 2004] (and these data) are plotted together with the field data by *Powell et al.* [2003]. The quantities of C_D in laboratory and field conditions are close, but the decrease of C_D for 10 m exceeding 35 m s^{-1} reported in *Powell et al.* [2003] was not observed. The differences between laboratory and field data are expectable due to strong differences in fetch. Besides, as it was reported in *Young* [2003], at hurricane conditions the wavefield is dominated by the swell generated in the regions of high winds, which is not reproduced in laboratory conditions. Since the fetches in the laboratory facilities are much lower than in the field conditions, then the waves in the lab are shorter and steeper than in the sea, an enhanced aerodynamic resistance of the water surface can be expected. The additional reason suggested by *Donelan et al.* [2004] reads that in laboratory facility the wind-wave interaction is studied in stationary conditions of spatially developing turbulent boundary layer, while in the field conditions, the wind in hurricane eye walls is strongly unsteady and represents an inhomogeneous flow.

2.3. Wavefield at Strong Winds in Laboratory Conditions

[19] Aerodynamic roughness of the sea surface is conditioned to waves at the water surface including strong wind conditions. According to *Powell* [2007], the surface drag depends significantly on the sector of the tropical cyclone, where it is measured. The sea surface drag is strongly enhanced in the left front sector of the tropical cyclone in comparison with the right and rare sector. *Powell* [2007] pointed out that although the data are insufficient for final conclusions, it seems that the aerodynamic drag depends on the wavefield, which is significantly different in different sectors of the tropical cyclone. In this paper the correlation of the wavefield parameters and aerodynamic surface resistance was investigated to elucidate the origin of the saturation of C_D with the wind growth.

[20] The wind-wave field parameters in the flume were measured by three wire gauges positioned in the corners of an equal side triangle with 2.5 cm side; the data sampling rate was 100 Hz. Three dimensional frequency-wave number spectra were retrieved from these data by the algorithm similar to the wavelet directional method (WDM) suggested by *Donelan et al.* [1996]. Time series of water elevation from the wave staffs were processed by the window FFT with the window width 2^N (N is an integer) without overlapping. The complex amplitudes of harmonics at each frequency ω: $A_\omega(x_n, y_n)\exp(i\varphi_\omega(x_n, y_n))$ were calculated, here $n = 1, 2, 3$ is the number of the wave staff. Suppose, that the wavefield is a superposition of harmonic waves with the wave numbers $\vec{k} = (k_x, k_y)$

$$A_\omega(x_n, y_n)\exp(i\varphi_\omega(x_n, y_n)) = \sum_{x,y} A_{x,y}(\omega)\exp\left(i\left(k_x x_n + k_y y_n\right)\right), \tag{9}$$

and one harmonic wave dominates in each interrogation window (the applicability of this supposition is verified below), then

$$\varphi_\omega(x_n, y_n) = k_x x_n + k_y y_n. \tag{10}$$

[21] And the wave number components can be calculated by the phase difference at different wave staffs

$$\Delta\varphi_{n,m} = \varphi_\omega(x_n, y_n) - \varphi_\omega(x_m, y_m). \tag{11}$$

[22] In these experiments three wave staffs were used, then

$$\begin{aligned} k_x &= \left(\Delta\varphi_{1,2}\Delta y_{1,3} - \Delta\varphi_{1,3}\Delta y_{1,2}\right)/\Delta, \\ k_y &= \left(\Delta\varphi_{1,3}\Delta x_{1,2} - \Delta\varphi_{1,2}\Delta x_{1,3}\right)/\Delta, \\ \Delta &= \Delta x_{1,2}\Delta y_{1,3} - \Delta x_{1,3}\Delta y_{1,2}. \end{aligned} \tag{12}$$

[23] To obtain the directional spectra the Cartesian coordinates (k_x, k_y) were transformed to the polar coordinates (k, θ) by $k_x = k\cos\theta$, $k_y = k\sin\theta$.

[24] Then 3-D frequency-wave number spectrum $S(\omega, k, \theta)$ was obtained similar to *Donelan et al.* [1996] by binning the

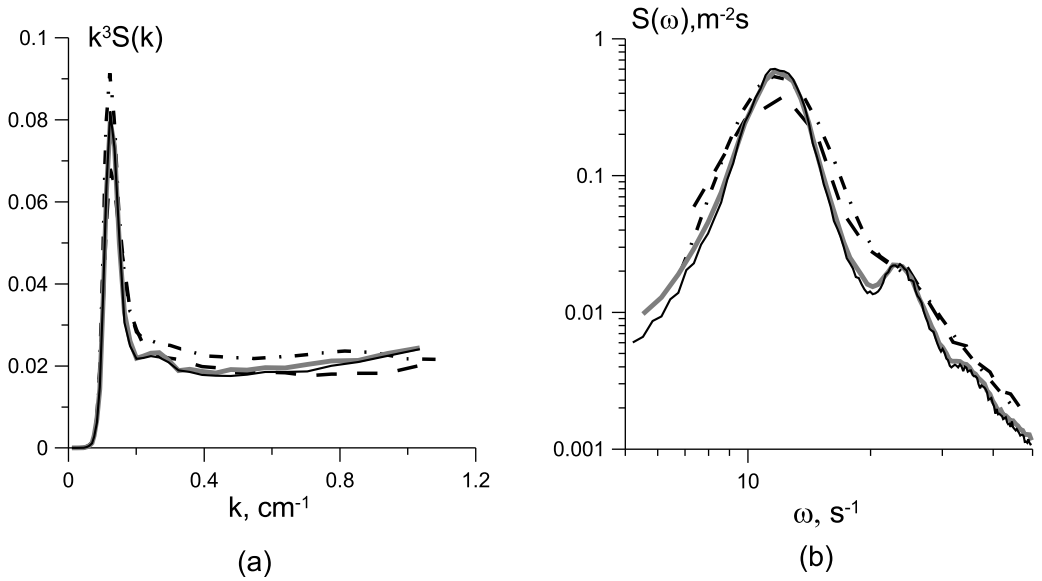

Figure 4. (a) Omnidirectional wave number saturation spectra and (b) frequency spectra. Obtained by the window FFT for the windows 1024 points (solid black line), 512 points (solid gray line), 128 points (dashed line), and by WDM (dash-dotted line).

amplitudes squared into calculated bins in k and θ. Integrating $S(\omega, k, \theta)$ over wave number or frequency yields frequency $S(\omega, \theta)$ or wave number $S(k, \theta)$ directional spectra respectively. Integrating over θ gives the omnidirectional frequency spectra and the wave number spectra correspondingly. The upper limit of the wave number spectrum is prescribed by the distance between the wave staffs d, $k_u = \pi/d$, in our experiments $k_u = 1.25$ cm^{-1}.

[25] The developed algorithm is based on the supposition that the dominating wavefield within the interrogation window at a given frequency ω is a harmonic wave, which is correct for a rather short time interval due to groupiness of the surface wavefield. To check the applicability of this supposition we investigated the dependence of the spectra on the width of the interrogation window. In Figure 4a an example of the omnidirectional wave number saturation spectra retrieved from the records of 3 waves staffs are shown for the windows of 128 points (1.28 s), 512 points (5.12 s) and 1024 points (10.24 s) widths, the total length of the record was about 800,000 points (8000 s). It is clear that the tenfold variation of the window width only slightly affects the wave number spectra. Besides, in Figure 4a the omnidirectional wave number saturation spectra retrieved from the same record by WDM algorithm [*Donelan et al.*, 1996] is shown. The difference between the spectra given by both algorithms is less than 15%. The advantage of high spectral resolution of the window FFT against the wavelet transformation illustrates Figure 4b, where frequency elevation spectra are plotted: the use of the 1024 point and 512 point windows of width even enabled us to resolve secondary peaks in frequency and wave number spectra, while the spectra obtained for 1024 point and 512 point windows are hardly discernable. Concerning these estimations, we used the algorithm based on the window FFT with the window width of 512 points (or 5.12 s).

[26] The wind-wave saturation spectra at different 10 m wind speeds U_{10} are plotted in Figure 5a. The presence of a sharp peak downshifting with the increasing wind speed and a long plato is typical for the measured spectra. The dependencies of main integral parameters of surface waves on the wind speed were investigated. In Figure 5 the significant wave height (*SWH*) (Figure 5b), peak wave number k_p (Figure 5c) and peak frequency ω_p (Figure 5d) are presented via 10 m wind speed. Curves are power best fitting of experimental points, which gives $SWH \sim U_{10}^{1.5}$, $k_p \sim U_{10}^{-1.45}$ and $\omega_p \sim U_{10}^{-0.72}$. As a result, the slope of the spectral peak proportional to the product of the significant wave height and the peak wave number ($S_p = k_p\, SWH/4$) only slightly depends on the wind speed (see Figure 6, open circles), that probably corresponds to the regime of the saturation of the peak waves similar to reported by *Donelan et al.* [2004]. The dependence of the peak frequency on the peak wave number was compared with the linear dispersion relation for free surface waves $\omega = \sqrt{gk}$ in Figure 5e. It is visible that the experimental frequencies of the waves are about 10% above those given by the linear dispersion relation. It can be explained by the cumulative effect of nonlinearity of the waves, wind drift flow and the wind.

[27] In Figure 6 we present the dependencies of the mean square slope on the wind velocity. The open circles show the mean square slope of the peak wave S_p. Other symbols present the mean square slope of the wavefield calculated according to the definition

$$Slope = \int_{k\,\min}^{k\,\max} k^2 S(k) dk, \tag{13}$$

where $S(k)$ is the omnidirectional elevation spectrum.

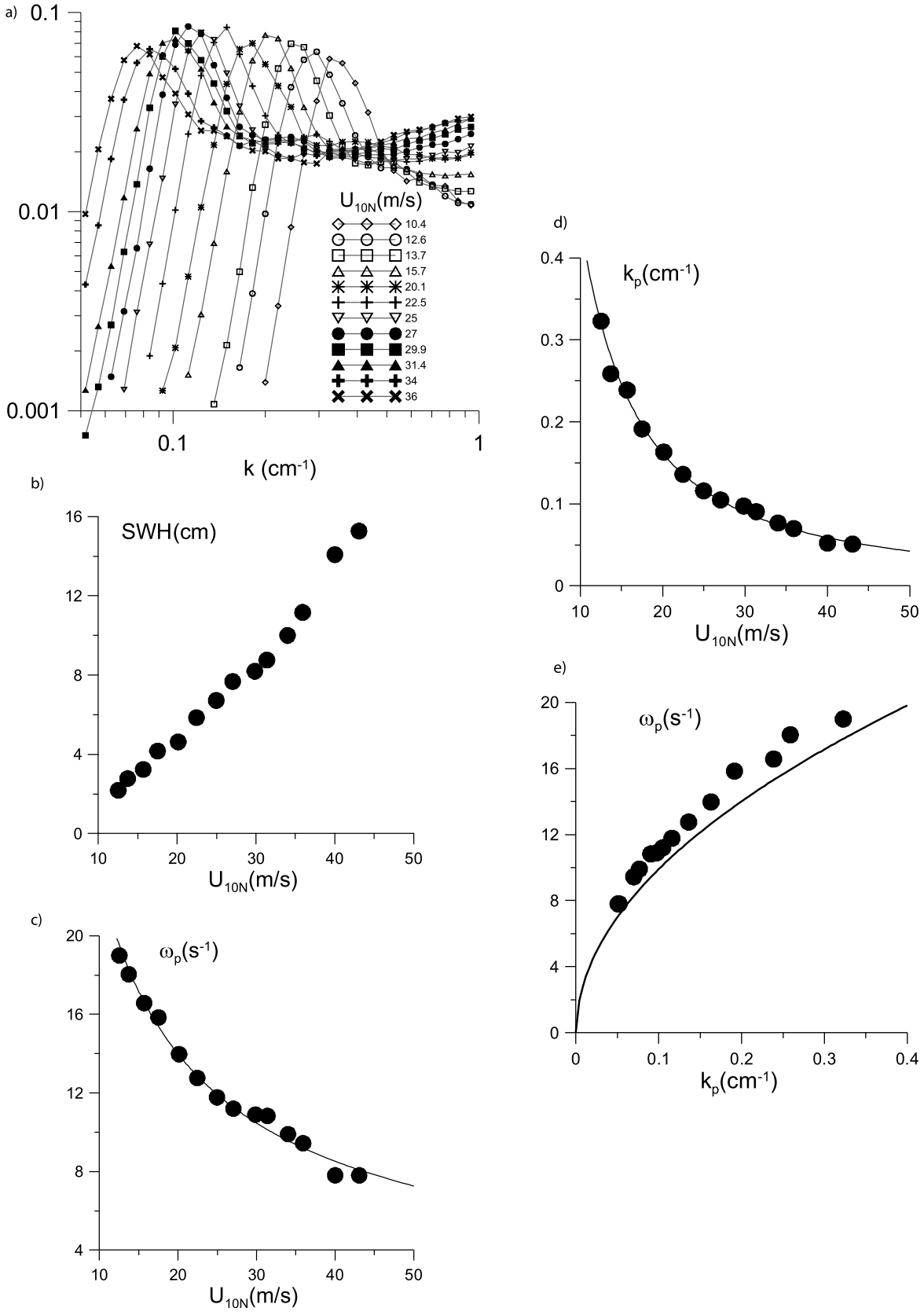

Figure 5. (a) Saturation wave number spectrum of the waves for a definite fetch (7 m) and different wind speeds U_{10}, (b) the dependence of the significant wave height on U_{10}, (c) the dependence of peak wave number on U_{10}, (d) the dependence of the peak wave frequency, and (e) the comparison of the dependence of the peak frequency on the peak wave number with the linear dispersion relation for free surface waves.

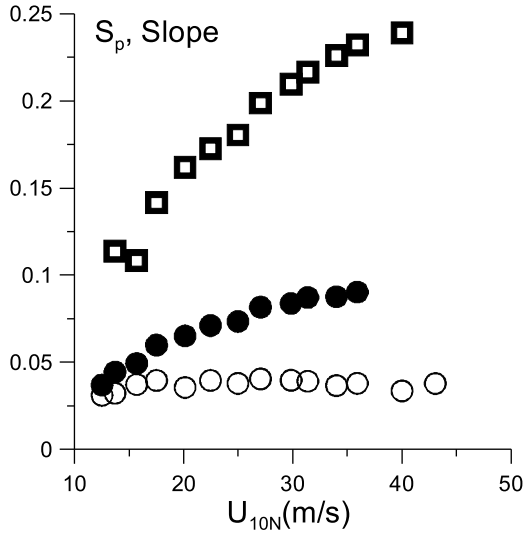

Figure 6. Dependences of the mean square slope on the wind velocity defined as $(a_p\ k_p)/2$ (open circles). The calculated accordingly integral (13) for $k_{max} = k_u$ (solid circles) and $k_{max} = 20\ m^{-1}$ (open squares).

[28] Here the upper limit $k_{min} = 0.01\ cm^{-1}$ was selected below the lowest wave number observed in the experiments. It is well known, that the integral (13) strongly depends on the upper limit k_{max}. Measurements with the array of 3 wave staffs provide $k_{max} = k_u = 1.25\ cm^{-1}$. The dependence $Slope(U_{10})$ for this upper limit is shown in Figure 6 by solid circles.

[29] To take into account the short wave ripples both generated near the crests of the waves due to wave breaking and excited by the wind, we continued the spectrum for $k > k_{max}$ by the model based on the ideas suggested by *Elfouhaily et al.* [1997]. The model omnidirectional spectrum $S(k)$ at $k > k_u$ is considered as a sum of low-frequency $S_l(k)$ and high-frequency $S_h(k)$ terms

$$S(k) = S_l(k) + S_h(k). \tag{14}$$

[30] The expression suggested by *Elfouhaily et al.* [1997] was taken to model $S_h(k)$:

$$S_h(k) = \frac{10^{-2}}{2}\left(1 + a\ln\frac{u_*}{c_m}\right)\frac{c_m}{c}e^{-\frac{1}{4}\left(\frac{k}{k_m}-1\right)^2},$$
$$a = \begin{cases} 1 & \text{for } u_* < 23\text{cm/s} \\ 3 & \text{for } u_* > 23\text{cm/s} \end{cases}. \tag{15}$$

Here $c_m = 23\ cm\ s^{-1}$, $k_m = c_m 2/g$.

[31] The low-frequency part $S_l(k)$ was continued for $k > k_u$ assuming the constant saturation spectrum, then

$$S_l(k) = \frac{\alpha}{k^3}.$$

[32] The constant α was selected from the condition, that at $k = k_u$ the model spectrum coincides with the measured one $S(k_u)$, then the omnidirectional spectrum at $k > k_u$

$$S(k) = (S_l(k_u) - S_h(k_u))\left(\frac{k_u}{k}\right)^3 + S_h(k). \tag{16}$$

[33] The angular dependence of the spectrum at $k > k_u$ was selected the same as it was measured at

$$k = k_u : f(\theta) = S(k_u, \theta)/S(k_u).$$

[34] The mean square slope calculated for the composite spectrum with the upper limit $k_{max} = 20\ cm^{-1}$ is shown by squares in Figure 6 as a function of U_{10}. Figure 6 clearly shows, that for both values of the upper limit k_{max} in the integral (13) the mean square slope tends to saturation when $U_{10} > 25\ m\ s^{-1}$. The comparison with the Figure 5a shows that the saturation spectrum as a whole demonstrates the tendency to saturation for $U_{10} > 25\ m\ s^{-1}$. It means that at the wind speed about 25 m s^{-1} the regime changing of the wavefield occurs. The comparison of the dependencies of the wave slope on the wind speed in Figure 6 and the drag coefficient dependency in Figure 3 shows, that the change in the wavefield regime correlated with the tendency to saturation of the surface drag dependence on the wind speed and Figure 7 clearly shows linear dependence between the surface drag coefficient and the mean square slope for both values of the upper limit k_{max} in the integral (13).

[35] The photos of the side views of the water surface (Figure 8) elucidate a possible origin of the change in the regime of the wavefield at 10 m wind speeds exceeding 25 m s^{-1}. Starting from this threshold, the wave breaking is intensified, because the crests of the waves are blown away by the strong tangential wind stress. It is accompanied with sprays, drops and bubbles near the wave crests, visible at the photos. Blowing away the crests of waves which steepness exceeds, a definite threshold leads to the effective

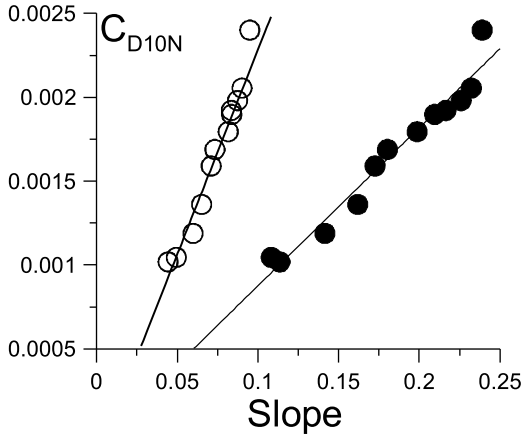

Figure 7. C_D against mean square slope diagram. Solid symbols are for $k_{max} = 20\ m^{-1}$ and open symbols are for $k_{max} = k_u$.

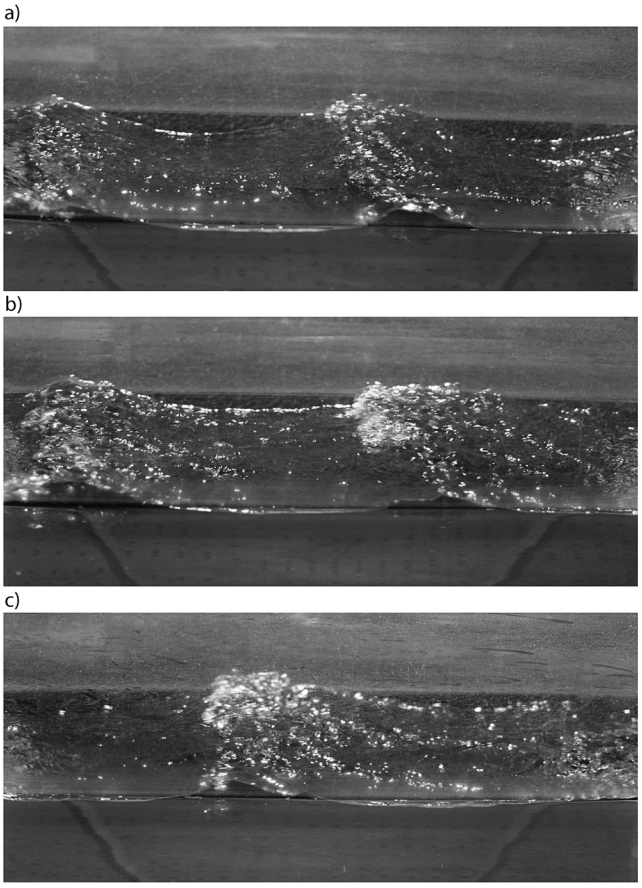

Figure 8. Examples of the wave images for different wind speeds U_{10}: (a) 22 m s^{-1}, (b) 25 m s^{-1}, and (c) 27 m s^{-1}. It is well seen that the intensive wave breaking with the foam on the crests starts from the wind speed 25 m s^{-1}.

smoothening of the waves, this leads to the saturation of the mean square slope of the wavefield. Basing on the theoretical model of the wind turbulent boundary layer over wavy water surface, we investigated, whether this wind smoothening of the surface is sufficient for the explanation of the surface drag saturation or not.

3. The Theoretical Model of the Aerodynamic Resistance of the Wavy Water Surface at Extreme Wind Conditions

[36] An important part of the aerodynamic resistance of the water surface is the form drag. Then the first step in the theoretical interpretation of the effect of the sea surface drag reduction at strong winds is the calculation of the surface form drag. This part of the total aerodynamic resistance describes the influence of the roughness of the surface. It can be expected that the smoothening of the water surface by a very strong wind significantly reduces the form drag and can possibly explain the experimental results. The wind over waves is modeled as a turbulent boundary layer within the first-order semiempirical model of turbulence based on the Reynolds equations closed with the Boussinesq hypothesis for turbulent stress with the self-similar eddy viscosity coefficient for the turbulent boundary layer

$$\nu = \nu_a f\left(\frac{u_* \eta}{\nu_a}\right), \tag{17}$$

where ν_a is the air molecular viscosity.

[37] We used the approximation for f obtained by *Smolyakov* [1973] on the basis of the laboratory experiments on a turbulent boundary layer over the aerodynamically smooth plate

$$\nu = \nu_a\left\{1 + \kappa\frac{u_* \eta}{\nu_a}\left[1 - e^{-\frac{1}{L}\left(\frac{u_* \eta}{\nu_a}\right)^2}\right]\right\}. \tag{18}$$

[38] In this expression L is a number, which determines the scale of the viscous sublayer of a turbulent boundary layer; it depends on the regime of the flow over the surface. This comparison with the parameters of the velocity profile in the turbulent boundary layer from *Miles* [1959] gives L = 22.4 for the aerodynamically smooth surface, L = 13.3 for the transition regime of a flow over surface, and L = 1.15 for the rough surface. Turbulent viscosity can be specified as $\nu_T = \nu - \nu_0$.

[39] To verify the applicability of the model we compared the results of the calculation of the wind-wave growth rates within this model and the viscoelastic model of the turbulence similar to one suggested by *Miles* [1996]. Expressions for the eddy viscosity coefficient were derived from the set of equations for the turbulent Reynolds stresses described in *Rodi* [1980]

$$\frac{\partial \sigma_{ij}}{\partial t} + \langle u_k\rangle \frac{\partial \sigma_{ij}}{\partial x_k} = -C_1\frac{\varepsilon}{b}\left(\sigma_{ij} - \frac{2}{3}b\delta_{ij}\right) + \kappa b\left(\frac{\partial\langle u_i\rangle}{\partial x_j} + \frac{\partial\langle u_j\rangle}{\partial x_i}\right) - \frac{2}{3}\varepsilon\delta_{ij}. \tag{19}$$

[40] Here b is the kinetic energy of turbulence, ϵ is the rate of dissipation of the kinetic energy of turbulence, C_1 = 1.5–2.2 is the empirical constant, b and ε relate to the turbulent viscosity as follows: $\nu_T \sim b^2/\varepsilon$.

[41] Linearizing (19), neglecting wave disturbances of b and ϵ and taking into account the relationship of the kinetic energy of turbulence and the turbulent stresses in a turbulent boundary layer gives for the wave disturbances of turbulent stresses $S_{ij} = \hat{S}_{ij}e^{-i(\omega t - kx)}$

$$S_{ij} = \nu_{wave}\left(\frac{\partial\langle u_i\rangle}{\partial x_j} + \frac{\partial\langle u_j\rangle}{\partial x_i}\right),$$

where

$$\nu_{wave} = \frac{\nu_T}{1 + \frac{\nu_T i(kU_0 - \omega)\alpha}{u_*^2}} \tag{20}$$

and α is a constant of order 1. Obvious generalization of (20), which takes into account the turbulent transport in the viscous sublayer is as follows:

$$\nu_{wave} = \nu_0 + \frac{\nu - \nu_0}{1 + i\frac{(\nu - \nu_0)(kU_0 - \omega)\alpha}{u_*^2}}. \tag{21}$$

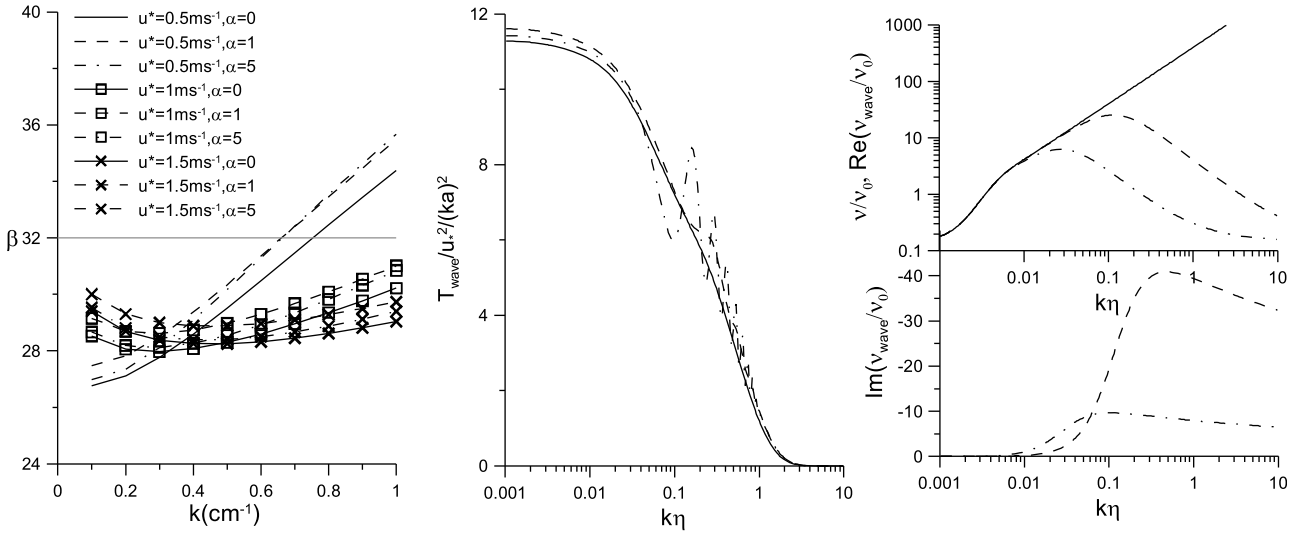

Figure 9. (left) Air-sea interaction parameter β via wave number calculated within the eddy viscosity model (19) and the model of viscoelastic turbulence (22), (middle) normalized profiles of the wave momentum flux (solid line, eddy viscosity model; dashed line, model of viscoelastic turbulence with $\alpha = 1$; dash-dotted line, $\alpha = 5$), and (right) profiles of the real and imaginary parts of effective viscosity coefficients.

[42] In Figure 9 (left) the dependencies of the wind-wave interaction parameter β in the definition of *Belcher et al.* [1994], which relates to the wind-wave growth rate as follows: $\mathrm{Im}\omega = \frac{1}{2}\left(\frac{u_*}{c}\right)^2 \beta\omega$, are presented for the parameters of wind and waves typical for this experiment. It is visible, that for the wave and wind parameters of these experiments β is not much sensitive to the model used in spite of the noticeable drop of effective complex viscosity (see Figure 9, right). It can be explained by Figure 9 (middle), where we presented the scaled wave momentum flux, which is mostly determined by the form drag of waves like the wind-wave interaction parameter β. The quantities of β are closed to the ones suggested by *Plant* [1982]:$\beta_{Plant} = 0.04 \pm 0.02$, $\frac{\rho_a}{\rho_w} = 1.25 \cdot 10^{-3}$ and $\beta = 32 \pm 16$. Basing on this, we used below a simpler model of eddy viscosity parameterization for the further analysis.

[43] The wind-wave interaction is considered here in the quasi-linear approximation similar to the approach developed by *Jenkins* [1992], *Janssen* [1989], and *Reutov and Troitskaya* [1995]. Then disturbances induced in the airflow by waves at the water surface are considered in the linear approximation (see equations (A16a)–(A16c)) and the only nonlinear effect taken into account is the wave momentum flux caused by the demodulation of wave-induced disturbances (see equation (A19)–(A21)). Let us discuss first the applicability of the suggested model for the description of the airflow over steep and breaking waves which occurred in the flume at strong winds. The main features of the model are as follows. It is based on the system of Reynolds equations with the first-order closing hypothesis. The wind-wave interaction is considered within the quasi-linear approximation, i.e., wave-induced disturbances in the airflow are considered in the linear approximation, but the resistive effect of the wave momentum flux on the mean flow velocity profile is taken into account, i.e., within the model the mean airflow over waves is treated as nonseparated.

[44] One can expect the existence of strong nonlinear phenomena such as sheltering, flow separation, etc., for the cases of steep and breaking waves. The structure of an airflow over waves has been recently investigated in detail by the method of Particle Image Velocimetry (PIV) [*Adrian*, 1991], when the flow is seeded with the small particles illuminated by the laser light and then taken with a digital camera. This technique was applied by *Reul et al.* [1999, 2008] and *Veron et al.* [2007] and clearly demonstrated the effect of the airflow separation from the crests of the waves and reattachment at the windward face of the wave on the instantaneous patterns of the vector velocity fields.

[45] It should be emphasized that the PIV technique provides an instant picture of the velocity field, but the flow separation in the turbulent boundary layer over a gravity wave is a strongly nonstationary process due to both the stochastic character of the airflow and the brevity of the breaking event, which usually occurs within a small part of the wave period [*Duncan et al.*, 1999]. At the same time, the models of the air-sea fluxes and the wind-wave growth exploit the wind flow parameters averaged over turbulent fluctuations. We combined the measurements of the instant airflow velocity fields over the surface waves with statistical averaging [*Troitskaya et al.*, 2011]. The statistical ensemble of such vector fields for subsequent averaging was obtained by means of high-speed video filming and processing of the video films by the PIV algorithm. Individual flow realizations manifested the typical features of flow separation similar to those obtained by *Kawai* [1981, 1982], *Reul et al.* [1999, 2008], and *Veron et al.* [2007]. The average parameters were retrieved by the phase averaging of the individual vector fields. The averaged flow patterns turn out to be smooth and slightly asymmetrical, with the minimum of

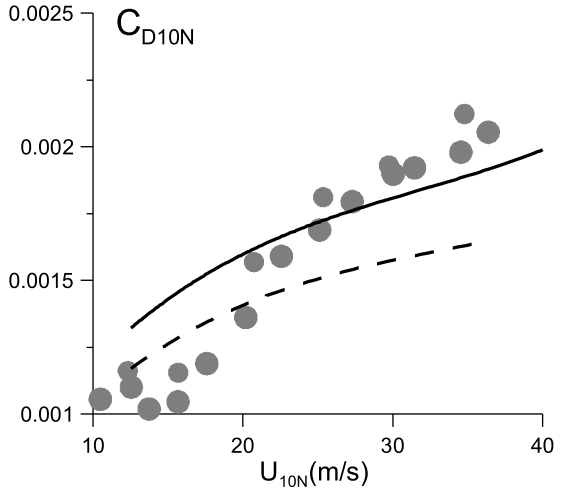

Figure 10. The dependence of the surface drag coefficient on the wind speed, comparing theory and the laboratory experiment. Circles, measurements; solid line, theoretical calculations with a short-wave spectrum of surface waves; dashed line, the neglected short-wave spectrum of surface waves.

the horizontal velocity near the water surface shifted to the leeward side of the wave profile.

[46] The results of these measurements were compared with the calculations within the quasi-linear model of the turbulent boundary layer described above. The wave parameters (wavelength, celerity, steepness), used in this comparison between the theory and the experiment, were retrieved from the same video films as those used for the airflow velocity calculations. The model calculations were in good agreement with the experimentally measured and conditionally averaged mean wind velocity, turbulent stress and also with the amplitude and phase of the main harmonics of the wave-induced velocity components [see *Troitskaya et al.*, 2011].

[47] Similarly, the applicability of the nonseparating quasi-linear theory for the description of average fields in the airflow over steep and even breaking waves, when the effect of separation is manifested at the instantaneous flow images was confirmed by DNS [*Yang and Shen*, 2010; *Druzhinin et al.*, 2012]. It can be qualitatively explained by strong intermittency of the flow separation observed in DNS. We were encouraged by these results to apply the quasi-linear model for the calculation of the form drag of the water surface at strong winds.

4. Comparison of Theoretical Prediction With Experimental Results: Discussion

[48] The form drag of the water surface was calculated within the model described above for the parameters (friction velocity and wave spectra) measured in the flume. At $k < k_u$ the three-dimensional elevation spectrum $S(\omega, k, \theta)$ was taken from the experimental data. At $k > k_u$ we used the approximation (16) with the *Elfouhaily et al.* [1997] spectrum (15). Special numerical tests showed, that the calculated values of the aerodynamic resistance were only slightly sensitive to the frequency dependence of the spectrum. Then in further calculations the real three-dimensional spectrum was replaced by the model one, in which the frequency dependence was taken as the delta function on the dispersion relation for free surface waves

$$S(\omega, k, \theta) = \delta(\omega - \omega(k)/2\pi)S(k, \theta).$$

[49] To investigate the sensitivity of the model to the spectrum of surface waves we calculated C_D, when the contribution of short surface waves was eliminated by a cutoff at the wave number 1.2 cm^{-1}.

[50] The obtained dependences of the drag coefficient on wind velocity are shown in Figure 10. It is clear that the model reproduces the tendency to saturation of the surface drag coefficient. Taking into account the short-wave part of the spectra yields quantitative agreement of the calculated and measured C_D. One of possible source of the differences between the calculated and measured dependences $C_D(U_{10})$ can be an inappropriate model of the high-frequency part of the wave spectra used in calculations, since the *Elfouhaily et al.* [1997] spectrum was adjusted for the sea, but not for lab conditions. Unfortunately, the measurement of the spectrum of short waves (cm and mm wavelength) with a high space resolution is a difficult problem especially at strong wings. The optical methods developed by *Jähne et al.* [2005] and *Rocholz and Jähne* [2010] are promising for laboratory conditions.

5. Conclusions

[51] The main objective of this work is the investigation of factors determining momentum exchange under high wind speeds basing on the laboratory experiment in a well-controlled environment. The experiments were carried out in the Thermo-Stratified Wind-Wave Tank (TSWIWAT) of the Institute of Applied Physics. The parameters of the facility are as follows: airflow 0–25 m s^{-1} (equivalent 10 m neutral wind speed U_{10} up to 40 m s^{-1}), dimensions 10 m × 0.4 m × 0.7 m, temperature stratification of the water layer. Simultaneous measurements of the airflow velocity profiles and wind waves were carried out in the wide range of wind velocities. Airflow velocity profile was measured by the scanning Pitot tube. The water elevation was measured by the three-channel wave gauge. Top and side views of the water surface were fixed by CCD camera.

[52] Wind friction velocity and the surface drag coefficients were retrieved from the measurements by the profile method. The obtained values are in good agreement with the data of measurements by *Donelan et al.* [2004]. The directional frequency-wave number spectra of the surface waves were retrieved by the algorithm similar to the wavelet directional method [*Donelan et al.*, 1996], but based on FFT. The obtained dependencies of the parameters of the wind waves indicate the existence of two regimes of the waves with the critical wind speed U_{cr} about 25 m s^{-1}. For $U_{10} > U_{cr}$ the mean square slope of wind waves demonstrated some tendency to saturation. The surface drag also tends to saturation for $U_{10} > U_{cr}$ similarly to *Donelan et al.* [2004]. Video filming indicates the onset of wave breaking with the white capping and spray generation at wind speeds

approximately equal to U_{cr}. Based on the experimental data, a possible physical mechanism of the drag is suggested. Tearing of the wave crests at severe wind conditions leads to the effective smoothing (decreasing wave slopes) of the water surface, which in turn reduces the aerodynamic roughness of the water surface.

[53] We compared the obtained experimental dependencies with the predictions of the quasi-linear model of the turbulent boundary layer over the waved water surface [*Reutov and Troitskaya*, 1995]. The comparison shows that the theoretical predictions give low estimates for the measured drag coefficient and wavefields. Taking into account momentum flux, associated with the high-frequency part of the wind-wave spectra, yields theoretical estimations in good agreement with the experimental data.

Appendix A

[54] The wind flow is described within the first-order semiempirical model of turbulence based on the set of the Reynolds equations

$$\frac{\partial\langle u_i\rangle}{\partial t}+\langle u_j\rangle\frac{\partial\langle u_i\rangle}{\partial x_j}+\frac{1}{\rho_a}\frac{\partial\langle p\rangle}{\partial x_i}=\frac{\partial\sigma_{ij}}{\partial x_j} \tag{A1}$$

and the following expressions for the tensor of turbulence stresses:

$$\sigma_{ij}=u_i'u_j'=\nu\left(\frac{\partial\langle u_i\rangle}{\partial x_j}+\frac{\partial\langle u_j\rangle}{\partial x_i}\right). \tag{A2}$$

[55] Here $\langle\ldots\rangle$ denotes the quantities averaged over turbulent fluctuations, ν is the turbulent viscosity coefficient, a given function of z. We use a self-similar expression for the eddy viscosity coefficient in the turbulent boundary layer expressed by equation (19).

[56] The boundary conditions at the air-sea interface $z = \xi(x, y, t)$ are

$$\frac{\partial\xi}{\partial t}+\langle u\rangle\frac{\partial\xi}{\partial x}+\langle v\rangle\frac{\partial\xi}{\partial y}\bigg|_{z=\xi(x,y,t)}=\langle w\rangle\bigg|_{z=\xi(x,y,t)}, \tag{A3}$$

$$\left\langle\vec{u}_\tau^{\,w}\right\rangle\big|_{z=\xi(x,y,t)}=\left\langle\vec{u}_\tau^{\,a}\right\rangle\big|_{z=\xi(x,y,t)}, \tag{A4}$$

$\langle u\rangle$, $\langle v\rangle$ are the x and y components of the velocity field in the air, averaged over turbulent fluctuations, $\left\langle\vec{u}_\tau^{\,w}\right\rangle=\left\langle\vec{u}_\tau^{\,a}\right\rangle$ are the tangential velocity components in water and in air, $\langle w\rangle$ is the z component of the velocity field in the air.

[57] The random field of the water surface elevation is presented as a Fourier-Stieltjes transform

$$\xi(\vec{r},t)=\int dA\left(\vec{k},\omega\right)e^{i\left(\vec{k}\vec{r}-\omega t\right)}, \tag{A5}$$

here $\vec{k}=\left(k_x,k_y\right)$ is a two-dimensional wave vector, ω is the frequency of surface waves.

[58] For a statistically homogeneous and stationary process the wave number-frequency spectrum $F\left(\vec{k},\omega\right)$ can be introduced as follows:

$$\left\langle dA\left(\vec{k},\omega\right)dA\left(\vec{k}_1,\omega_1\right)\right\rangle=F\left(\vec{k},\omega\right)\delta\left(\vec{k}-\vec{k}_1\right)\delta(\omega-\omega_1)d\vec{k}d\vec{k}_1d\omega d\omega_1. \tag{A6}$$

[59] To avoid strong geometric nonlinearity, the transformation to the wave-following curvilinear coordinates is performed

$$\begin{aligned}x&=\zeta_1+\int i\cos\vartheta\, e^{i(k(\zeta_1\cos\vartheta+\zeta_2\sin\vartheta)-\omega t)-k\eta-i\varphi}dA,\\ y&=\zeta_2+\int i\sin\vartheta\, e^{i(k(\zeta_1\cos\vartheta+\zeta_2\sin\vartheta)-\omega t)-i\varphi-k\eta}dA,\\ z&=\eta+\int e^{i(k(\zeta_1\cos\vartheta+\zeta_2\sin\vartheta)-\omega t)-i\varphi-k\eta}dA,\end{aligned} \tag{A7}$$

here θ is the angle between the wave number wave vector $\vec{k}$ and direction of x axis. In the linear approximation the coordinate surface $\eta = 0$ coincides with the waved water surface.

[60] The solution to the set of the Reynolds equations (A1) is searched as a superposition of mean wind field $\vec{U}_0(\eta)$ and the disturbances induced in the airflow by the waves at the water surface. Then, the velocity field is as follows:

$$\langle\vec{u}\rangle=\vec{U}_0(\eta)+\int\vec{u}'(\eta)e^{i(k(\zeta_1\cos\vartheta+\zeta_2\sin\vartheta)-\omega t)-i\varphi-k\eta}kdA. \tag{A8}$$

[61] The wind-wave interaction is considered here in the quasi-linear approximation similar to the approach developed by *Jenkins* [1992], *Janssen* [1989], and *Reutov and Troitskaya* [1995]. Then the wave disturbances induced in the airflow by the waves at the water surface are described in the linear approximation and can be considered independently. The coordinate transformation (A7) can be considered as a superposition of formal coordinate transformations for each single harmonic. Nonlinear terms or wave momentum fluxes enter into the equations for the components of mean velocity.

[62] Considering first equations for the disturbances, induced by a single harmonic wave at the water surface with the wave vector $\vec{k}$, frequency ω and amplitude dA, we introduce the formal coordinate transformation, where the coordinate line $\eta = 0$ coincides with the water surface disturbed by this single harmonic wave

$$\begin{aligned}x&=\zeta_1+i\cos\vartheta e^{i(k(\zeta_1\cos\vartheta+\zeta_2\sin\vartheta)-\omega t)-k\eta-i\varphi}dA,\\ y&=\zeta_2+i\sin\vartheta e^{i(k(\zeta_1\cos\vartheta+\zeta_2\sin\vartheta)-\omega t)-k\eta-i\varphi}dA,\\ z&=\eta+e^{i(k(\zeta_1\cos\vartheta+\zeta_2\sin\vartheta)-\omega t)-i\varphi-k\eta}dA.\end{aligned} \tag{A9}$$

[63] The linear coordinate transformation

$$\begin{aligned}\zeta'_1&=\zeta_1\cos\vartheta+\zeta_2\sin\vartheta-\frac{\omega}{k}t,\\ \zeta'_2&=\zeta_2\cos\vartheta-\zeta_1\sin\vartheta=y_2\cos\vartheta-y_1\sin\vartheta=y'\end{aligned}, \tag{A10}$$

defines the reference frame following this harmonic wave, where the wavefield does not depend on ζ'_2 (or Cartesian

coordinate y'), i.e., it depends only on two coordinates ζ_1' and η. Tangential velocity components are transformed similar to (A10), and in the new reference frame

$$u' = u\cos\vartheta + v\sin\vartheta - \frac{\omega}{k}, \quad v' = -u\sin\vartheta + v\cos\vartheta. \tag{A11}$$

[64] It means that the stream function Φ can be introduced for the motions in the plane $\zeta_2' = y' = const$ as follows:

$$u' = \frac{\partial\Phi}{\partial\eta},\ w' = -\frac{\partial\Phi}{\partial\zeta_1'} \tag{A12}$$

and the Reynolds equations can be formulated in terms of stream function Φ and vorticity χ

$$\frac{\partial\chi}{\partial t} + \frac{1}{I}\frac{\partial\chi}{\partial\zeta_1'}\left(\frac{\partial\Phi}{\partial\eta}\right) - \frac{1}{I}\frac{\partial\chi}{\partial\eta}\left(\frac{\partial\Phi}{\partial\zeta_1'}\right) = \Delta(\nu\chi) - \frac{2}{I^2}\nu_{\eta\eta}\frac{\partial^2\Phi}{\partial\zeta_1'^2} - -\frac{I_\eta}{I^3}\left(\left(\Phi_\eta\nu_\eta\right)_\eta - \nu_\eta\Phi_{\zeta_1'\zeta_1'}\right) - \frac{I_{\zeta_1'}}{I^3}\left(2\nu_\eta\Phi_{\zeta_1'\eta} - \Phi_{\zeta_1'}\nu_{\eta\eta}\right) + \Phi_\eta\nu_\eta\frac{I_{\zeta_1'}^2 + I_\eta^2}{I^4}, \tag{A13a}$$

$$\Delta\Phi = \chi = \frac{1}{I}\left(\Phi_{\zeta_1'\zeta_1'} + \Phi_{\eta\eta}\right) \tag{A13b}$$

here I is the Jacobian of transformation (A9). The transversal velocity component v' does not enter the equations (A13a) and (A13b), and v' obeys the following equation:

$$\frac{\partial v'}{\partial t} + \frac{1}{I}\left(\frac{\partial v'}{\partial\zeta_1'}\frac{\partial\Phi}{\partial\eta} - \frac{\partial v'}{\partial\eta}\frac{\partial\Phi}{\partial\zeta_1'}\right) = \Delta(v'\nu) + \frac{1}{I}v'_\eta\nu_\eta. \tag{A14}$$

[65] We search the solution to the system (A13a)–(A14) as a superposition of the mean field and harmonic wave disturbance

$$\Phi = \int\left(U_0(\eta)\cos\vartheta + V_0(\eta)\sin\vartheta - \frac{\omega}{k}\right)d\eta + \Phi_1(\eta)dA\,e^{ik\zeta_1'}, \quad v = V_0(\eta)\cos\vartheta - U_0(\eta)\sin\vartheta + V_1(\eta)dA\,e^{ik\zeta_1'}, \tag{A15a}$$

$$\chi = U_{0\eta}\cos\vartheta + V_{0\eta}\sin\vartheta + X_1(\eta)dA\ \ e^{ik\zeta_1'}. \tag{A15b}$$

[66] Equations for complex amplitudes $\Phi_1(\eta)$, $\chi_1(\eta)$, $V_1(\eta)$ are obtained by the linearization of the system (A13a)–(A14)

$$\left(\Phi_{0\eta}X_1 - \Phi_1\chi_{0\eta}\right)ik - \left(\frac{d^2}{d\eta^2} - k^2\right)(X_1\nu) = -2\nu_\eta\Phi_1k^2 - 2kAe^{-k\eta}\left(\Phi_{0\eta}\nu_\eta\right)_\eta, \tag{A16a}$$

$$\frac{d^2\Phi_1}{d\eta^2} - k^2\Phi_1 = X_1 - 2ke^{-k\eta}\Phi_{0\eta\eta}, \tag{A16b}$$

$$\left(\Phi_{0\eta}V_1 - \Phi_1V_\eta\right)ik = \nu\left(\frac{d^2}{d\eta^2} - k^2\right)V_1 + \nu_\eta V_{1\eta}k^2. \tag{A16c}$$

[67] We consider the solutions to the system (A15a)–(A16)) decreasing at large distances from the surface, i.e.,

$$\Phi_1\big|_{\eta\to\infty}\to 0; \quad V_1\big|_{\eta\to\infty}\to 0. \tag{A17}$$

[68] The boundary conditions at the water surface for the system (A16) follow from (A4) and (A5) are expressed in curvilinear coordinates [see *Reutov and Troitskaya*, 1995] for details

$$\Phi_1\big|_{\eta=0} = 0; \quad \Phi_{1\eta}\big|_{\eta=0} = 2\omega; \quad V_1\big|_{\eta\to 0} = 0. \tag{A18}$$

[69] The only nonlinear effect taken into account in the quasi-linear approximation is the demodulation of the wave disturbances induced in the airflow by waves at the water surface. Equations for mean velocity profile components $U_0(\eta)$ and $V_0(\eta)$ are obtained by the following steps. Averaging (A13a) and (A13b) over ζ_1' gives the equation for Φ_0 and averaging (A14) yields the equation for $\nu_0(\eta)$. Expressing $U_0(\eta)$ and $V_0(\eta)$ via $\Phi_0(\eta)$ and $\nu_0(\eta)$ by inversion (A15a) and (A15b) and integrating over the wind-wave spectrum gives

$$\frac{d}{d\eta}\left(\nu\frac{d(U_0, V_0)}{d\eta}\right) = \int\left(\tau_\parallel(\eta,k,\varphi,\omega)(\eta)\begin{pmatrix}\cos\varphi\\ \sin\varphi\end{pmatrix} + \tau_\perp(\eta,k,\varphi,\omega)(\eta)\begin{pmatrix}-\sin\varphi\\ \cos\varphi\end{pmatrix}\right)\cdot k^2F(k,\varphi,\omega)kdkd\varphi d\omega, \tag{A19}$$

here $\tau_\parallel(\eta, k, \theta, \omega)(\eta)$, $\tau_\perp(\eta, k, \theta, \omega)(\eta)$ are the components of the wave momentum flux induced by the surface wave with the wave number k, frequency ω propagating at the angle θ to the wind.

[70] The expression for $\tau_\parallel(\eta, k, \theta, \omega)(\eta)$ follows from (A13a) and (A13b)

$$\tau_\parallel(\eta,k,\varphi,\omega)(\eta) = k\left[k\nu_\eta\mathrm{Re}\left(\Phi_{1\eta} - k\Phi_1\right)e^{-k\eta} + 2k^2e^{-2k\eta}\nu_\eta U_0\cos\varphi\right] \tag{A20}$$

and the expression for $\tau_\perp(\eta, k, \theta, \omega)(\eta)$ follows from (A14):

$$\tau_\perp(\eta,k,\omega) = -\frac{1}{2}k\frac{d}{d\eta}\mathrm{Im}\left(\Phi_1^*V_1\right). \tag{A21}$$

[71] Equations (A19) express the conservation law for the vertical flux of two projections of the horizontal momentum component in the turbulent boundary layer. If the turbulent shear stress at a large distance from the surface is directed along x, the conservation law for the mean momentum components may be written as follows:

$$\tau_{turb}^{(x)}(\eta) + \tau_{1\parallel}(\eta) = u_*^2 \tag{A22}$$

$$\tau_{turb}^{(y)}(\eta) + \tau_\perp(\eta) = 0. \tag{A23}$$

[72] **Acknowledgments.** We are grateful to S. S. Zilitinkevich, G. G. Golytsyn, and V. N. Kudryavtsev for fruitful discussion and constructive criticism. This work was supported by a grant from the Government of the Russia Federation designed to support scientific research projects implemented under the supervision of leading scientists at Russian institutions of

higher learning (project code 11.G34.31.0048); grants RFBR 10-05-00339, 09-05-00779, and 11-08-97067; FTP scientific and scientific pedagogical cadres of 343 innovative Russia and FTP investigations in priority-driven directions of the modernization of Russian scientific technology complex; and President grant for young scientists MK-5575.2012.5.

References

Adrian, R. J. (1991), Particle imaging techniques for experimental fluid mechanics, *Annu. Rev. Fluid Mech.*, *23*, 261–304, doi:10.1146/annurev.fl.23.010191.001401.

Andreas, E. L. (2004), Spray stress revised, *J. Phys. Oceanogr.*, *34*(6), 1429–1440, doi:10.1175/1520-0485(2004)034<1429:SSR>2.0.CO;2.

Andreas, E. L., and K. A. Emanuel (2001), Effects of sea spray on tropical cyclone intensity, *J. Atmos. Sci.*, *58*(24), 3741–3751, doi:10.1175/1520-0469(2001)058<3741:EOSSOT>2.0.CO;2.

Barenblatt, G. I., and G. S. Golitsyn (1974), Local structure of mature dust storms, *J. Atmos. Sci.*, *31*(7), 1917–1933, doi:10.1175/1520-0469(1974)031<1917:LSOMDS>2.0.CO;2.

Belcher, S. E., J. A. Harris, and R. L. Street (1994), Linear dynamics of wind waves in coupled turbulent air-water flow. Part 1. Theory, *J. Fluid Mech.*, *271*, 119–151, doi:10.1017/S0022112094001710.

Donelan, M. A., W. M. Drennan, and A. K. Magnusson (1996), Nonstationary analysis of the directional properties of propagating waves, *J. Phys. Oceanogr.*, *26*, 1901–1914, doi:10.1175/1520-0485(1996)026<1901:NAOTDP>2.0.CO;2.

Donelan, M. A., B. K. Haus, N. Reul, W. J. Plant, M. Stiassnie, H. C. Graber, O. B. Brown, and E. S. Saltzman (2004), On the limiting aerodynamic roughness of the ocean in very strong winds, *Geophys. Res. Lett.*, *31*, L18306, doi:10.1029/2004GL019460.

Druzhinin, O. A., Y. I. Troitskaya, and S. S. Zilitinkevich (2012), Direct numerical simulation of a turbulent wind over 21 a wavy water surface, *J. Geophys. Res.*, *117*, C00J05, doi:10.1029/2011JC007789.

Duncan, J. H., H. Qiao, V. Philomin, and A. Wenz (1999), Gentle spilling breakers: Crest profile evolution, *J. Fluid Mech.*, *379*, 191–222, doi:10.1017/S0022112098003152.

Elfouhaily, T. B., B. Chapron, K. Katsaros, and D. Vandemark (1997), A unified directional spectrum for long and short wind-driven waves, *J. Geophys. Res.*, *107*, 15,781–15,796, doi:10.1029/97JC00467.

Emanuel, K. A. (1995), Sensitivity of tropical cyclones to surface exchange coefficients and a revised steady-state model incorporating eye dynamics, *J. Atmos. Sci.*, *52*(22), 3969–3976, doi:10.1175/1520-0469(1995)052<3969:SOTCTS>2.0.CO;2.

Fairall, C. W., E. F. Bradley, J. E. Hare, A. A. Grachev, and J. B. Edson (2003), Bulk parameterization of air-sea fluxes: Updates and verification for the COARE algorithm, *J. Clim.*, *16*(4), 571–591, doi:10.1175/1520-0442(2003)016<0571:BPOASF>2.0.CO;2.

Hara, T., and S. E. Belcher (2004), Wind profile and drag coefficient over mature ocean surface wave spectra, *J. Phys. Oceanogr.*, *34*(11), 2345–2358, doi:10.1175/JPO2633.1.

Hinze, J. O. (1959), *Turbulence: An Introduction to Its Mechanism and Theory*, 586 pp., McGraw-Hill, New York.

Jähne, B., M. Schmidt, and R. Rocholz (2005), Combined optical slope/height measurements of short wind waves: Principles and calibration, *Meas. Sci. Technol.*, *16*, 1937–1944, doi:10.1088/0957-0233/16/10/008.

Janssen, P. A. E. M. (1989), Wave-induced stress and the drag of air flow over sea waves, *J. Phys. Oceanogr.*, *19*(6), 745–754.

Janssen, P. A. E. M. (1991), Quasi-linear theory of wind wave generation applied to wave forecasting, *J. Phys. Oceanogr.*, *21*(11), 1631–1642, doi:10.1175/1520-0485(1991)021<1631:QLTOWW>2.0.CO;2.

Jarosz, E., D. A. Mitchell, D. W. Wang, and W. J. Teague (2007) Bottom-up determination of air-sea momentum exchange under a major tropical cyclone, *Science*, *315*, 1707–1709, doi:10.1126/science.1136466.

Jenkins, A. D. (1992), Quasi-linear eddy-viscosity model for the flux of energy and momentum to wind waves using conservation-law equations in a curvilinear coordinate system, *J. Phys. Oceanogr.*, *22*(8), 843–858, doi:10.1175/1520-0485(1992)022<0843:AQLEVM>2.0.CO;2.

Kawai, S. (1981), Visualization of air flow separation over wind wave crest under moderate wind, *Boundary Layer Meteorol.*, *21*, 93–104, doi:10.1007/BF00119370.

Kawai, S. (1982), Structure of air flow separation over wind wave crest, *Boundary Layer Meteorol.*, *23*, 503–521, doi:10.1007/BF00116275.

Kudryavtsev, V. N. (2006), On the effect of sea drops on the atmospheric boundary layer, *J. Geophys. Res.*, *111*, C07020, doi:10.1029/2005JC002970.

Kudryavtsev, V., and V. Makin (2007), Aerodynamic roughness of the sea surface at high winds, *Boundary Layer Meteorol.*, *125*, 289–303, doi:10.1007/s10546-007-9184-7.

Kudryavtsev, V., and V. Makin (2011), Impact of ocean spray on the dynamics of the marine atmospheric boundary layer, *Boundary Layer Meteorol.*, *140*, 383–410, doi:10.1007/s10546-011-9624-2.

Kukulka, T., T. Hara, and S. E. Belcher (2007), A model of the air-sea momentum flux and breaking-wave distribution for strongly forced wind waves, *J. Phys. Oceanogr.*, *37*(7), 1811–1828, doi:10.1175/JPO3084.1.

Large, W. G., and S. Pond (1981), Open ocean momentum flux measurements in moderate to strong winds, *J. Phys. Oceanogr.*, *11*(3), 324–336, doi:10.1175/1520-0485(1981)011<0324:OOMFMI>2.0.CO;2.

Makin, V. K. (2005), A note on drag of the sea surface at hurricane winds, *Boundary Layer Meteorol.*, *115*(1), 169–176, doi:10.1007/s10546-004-3647-x.

Makin, V. K., V. N. Kudryavtsev, and C. Mastenbroek (1995), Drag of the sea surface, *Boundary Layer Meteorol.*, *73*, 159–182, doi:10.1007/BF00708935.

Miles, J. W. (1959), On the generation of surface waves by shear flows. Part 2, *J. Fluid Mech.*, *6*, 568–582, doi:10.1017/S0022112059000830.

Miles, J. (1996), Surface-wave generation: A visco-elastic model, *J. Fluid Mech.*, *322*, 131–145, doi:10.1017/S002211209600273X.

Plant, W. J. (1982), A relationship between wind stress and wave slope, *J. Geophys. Res.*, *87*, 1961–1967, doi:10.1029/JC087iC03p01961.

Powell, M. D. (2007), Drag coefficient distribution and wind speed dependence in tropical cyclones, final report, Atl. Oceanogr. and Meteorol. Lab., Natl. Oceanic and Atmos. Admin., Key Biscayne, Fla.

Powell, M. D., P. J. Vickery, and T. A. Reinhold (2003), Reduced drag coefficient for high wind speeds in tropical cyclones, *Nature*, *422*, 279–283, doi:10.1038/nature01481.

Reul, N., H. Branger, and G. P. Giovanangeli (1999), Air flow separation over unsteady breaking waves, *Phys. Fluids*, *11*(7), 1959–1961, doi:10.1063/1.870058.

Reul, N., H. Branger, and J.-P. Giovanangeli (2008), Air flow structure over short-gravity breaking water waves, *Boundary Layer Meteorol.*, *126*, 477–505, doi:10.1007/s10546-007-9240-3.

Reutov, V. P., and Y. I. Troitskaya (1995), On the nonlinear effects in the interaction of gravity waves with turbulent airflow, *Izv. Russ. Acad. Sci. Atmos. Oceanic Phys.*, *31*(6), 825–834.

Rocholz, R., and B. Jähne (2010), Spatio-temporal measurements of short wind water waves, *Geophys. Res. Abstr.*, *12*, EGU2010-5509.

Rodi, W. (1980), Models for environmental turbulence, in *Prediction Methods for Turbulent Flows*, edited by W. Kollmann, pp. 227–322, Hemisphere Publ., Washington, D. C.

Smolyakov, A. V. (1973), Spectrum of the quadruple radiation of the plane turbulent boundary layer, *Acoust. Phys.*, *19*(3), 420–425.

Taylor, P. K., and M. J. Yelland (2001), The dependence of sea surface roughness on the height and steepness of the waves, *J. Phys. Oceanogr.*, *31*(2), 572–590.

Troitskaya, Y. I., and G. V. Rybushkina (2008), Quasi-linear model of interaction of surface waves with strong and hurricane winds, *Izv. Russ. Acad. Sci. Atmos. Oceanic Phys.*, *44*(5), 621–645, doi:10.1134/S0001433808050083.

Troitskaya, Y., D. Sergeev, O. Ermakova, and G. Balandina (2011), Statistical parameters of the air turbulent boundary layer over steep water waves measured by the PIV technique, *J. Phys. Oceanogr.*, *41*, 1421–1454, doi:10.1175/2011JPO4392.1.

Veron, F., G. Saxena, and S. K. Misra (2007), Measurements of the viscous tangential stress in the airflow above wind waves, *Geophys. Res. Lett.*, *34*, L19603, doi:10.1029/2007GL031242.

Yang, D., and L. Shen (2010), Direct-simulation-based study of turbulent flow over various waving boundaries, *J. Fluid Mech.*, *650*, 131–180, doi:10.1017/S0022112009993557.

Young, I. R. (2003), A review of the sea state generated by hurricanes, *Mar. Struct.*, *16*, 201–218, doi:10.1016/S0951-8339(02)00054-0.